

Sub-Nyquist SAR via Fourier Domain Range Doppler Processing

Kfir Aberman, and Yonina C. Eldar, *Fellow, IEEE*

Abstract—Conventional Synthetic Aperture Radar (SAR) systems are limited in their ability to fulfill the increasing demand for improved spatial resolution and wider coverage. While the former demand requires high sampling rates which are difficult to attain in practice, the latter is upper bounded due to the Nyquist theorem. Consequently, sampling rate reduction is of high practical value in radar imaging. In this paper, we introduce a new algorithm, equivalent to the well-known Range-Doppler method, to process SAR data using the Fourier series coefficients of the raw signals. Using the framework of compressed sensing (CS), we then demonstrate how to exploit the new algorithm features to reduce sampling rate in both range and azimuth axes and process the signals effectively at sub-Nyquist rates. We show that an image can be reconstructed after dropping a large percentage of the transmitted pulses, with no resolution degradation and suggest exploiting the complementary pulses to capture other scenes within the same coherent processing interval (CPI) using electronic beam steering. The proposed recovery algorithms exploit the inherent two-dimensional structure of the problem and form a new CS-SAR imaging method that can be applied to high-quality and high-resolution real SAR imaging data acquired at sub-Nyquist rates in both axes. The performance of our algorithms is assessed using simulated and real data sets. Finally, our approach is implemented in hardware using a previously suggested Xampling radar prototype.

Index Terms—synthetic aperture radar (SAR), compressed sensing, sparse recovery, sub-Nyquist sampling.

I. INTRODUCTION

SYNTHETIC aperture radar (SAR) is a well proven radar imaging technology that enables the production of high-resolution images of targets and terrain. SAR can be operated at night and in adverse weather conditions, overcoming limitations of optical and infrared systems. The basic idea of SAR is that a single monostatic radar transmits pulses at microwave frequencies at a uniform pulse repetition interval (PRI) as it moves along a path. The echoes coming from ground scatterers are then collected and processed in order to generate a focused image. The coherent information recorded at the different positions is used to synthesize a long antenna in order to improve resolution.

Processing of SAR data requires two-dimensional space-variant correlation of the raw data with the point scatter response of the SAR data acquisition system [1]. A full two-dimensional time domain correlation can handle the space-variant, but is computationally inefficient. In order to accelerate computation time, various algorithms have been developed that impose different approximations on the correlation kernel

[2], [3]. The Range-Doppler Algorithm (RDA) is the most widely used approach for high resolution processing of SAR data. It is conceptually the simplest, can accommodate range varying parameters and is independent of the transmitted pulse structure. An important part of RDA is the Range Cell Migration Correction (RCMC) operation, which is aimed at decoupling the dependency between the two dimensions of the system, range and azimuth, which are also known as fast-time and slow-time, respectively. This step requires fine delay resolution in the Range-Doppler domain, which is typically obtained by digital interpolation [4]. Interpolation allows to reduce the sampling rate at the cost of additional digital computations which effectively increase the rate in the digital domain. In practice, oversampling is then employed to eliminate artifacts caused by digital implementation of standard RDA processing.

According to the Shannon-Nyquist theorem, the minimal sampling rate at the SAR receiver should be at least twice the bandwidth of the detected signal in order to avoid aliasing [5]. In addition, the need to avoid azimuth ambiguities in the resulting image is translated into a minimal pulse repetition frequency (PRF) requirement. The PRF has to be greater than the Doppler bandwidth of the received signals which is dictated by several system parameters, i.e. platform velocity, carrier frequency and the real antenna aperture. This, in fact, limits the maximal swath of the system [6]. Moreover, in order to capture a scene, the Nyquist criterion requires that all the coherent information within the coherent processing interval (CPI), which equals the product of the number of transmitted pulses and the PRI, will be considered during processing. Consequently, this two-dimensional dense sampling results in large data rates, requiring large on board memory which may be restricted by downlink throughput requirements, especially for orbital missions.

The emerging theory of compressive sensing (CS) states that a signal which is sparse in some basis, can be reconstructed from highly incomplete samples or measurements [7]–[9]. Since a SAR image is a map of a spatial distribution of the reflectivity function of stationary targets and terrain, many SAR images can be sparse or compressible under an appropriate basis such as wavelet, curvelet or total variation [10]. CS can be applied on both dimensions of SAR. While rate reduction in range is realized by low rate analog-to-digital conversion (ADC) at the receiver, azimuth subsampling is expressed by the transmission of a smaller number of pulses during a CPI.

CS theory has shown promising results in the field of sub-Nyquist sampling in radar applications. The use of Fourier series coefficients in pulse-Doppler radar enables practical sub-Nyquist sampling when the illuminated scene consists of

This project has received funding from the European Union’s Horizon 2020 research and innovation program under grant agreement No. 646804-ERC-COG-BNYQ, and from the Israel Science Foundation under Grant no. 335/14.

moving targets that correspond to a sparse range-Doppler map [11]–[13]. CS has also been explored in a wide range of radar imaging applications [14]. In [15], the authors applied CS on SAR images by separating the processing into two decoupled one-dimensional operations. They showed that CS theory can then be applied in order to reduce the rate in azimuth. However, since RCMC is ignored, this method does not consider system setups with range varying parameters, hence, the quality of some images might be degraded.

The authors in [16] and [17] used CS in order to reduce the rate in both dimensions. In [16] RDA and CS were combined in order to exploit RDA benefits, however, only linear interpolation was consumed. To achieve accurate results, the data is normally oversampled and the kernel of the interpolator should span many samples which comes at the expense of efficiency and computational load. In [17], due to its simplicity, the authors suggest a compressive sensing algorithm based on the Chirp Scaling Algorithm (CSA). This processing technique does not require interpolation [3]. Unlike RDA, this method is based on the assumption that the transmitted signal has a chirp form and is known to be less robust to noise. Both methods apply random sampling in time without proposing a practical sampling mechanism which enables the extraction of the low-rate samples directly from the analog signals.

Following subsampling, most of the existing CS imaging schemes stack the whole two-dimensional reflectivity map into a vector in order to apply CS recovery methods. For real SAR images, this vectorization operation results in large memory requirements and long reconstruction times. Alternatively, the authors in [18] suggested to split the image into segments and use several computing units to process the data in parallel and solve the vectorized CS problem.

Our main contribution is divided into two parts. First, we present a new algorithm, equivalent to RDA, which handles the burden of time interpolation via Fourier series coefficients. Our approach is based on a technique recently developed for ultrasound imaging, called beamforming in frequency [19], [20]. This method shows that conventional beamforming in time which is used to process ultrasound signals can be equivalently performed in the Fourier domain. Adapting this concept to SAR, the required non-integer non-constant shifts in the RCMC stage can be performed in frequency using similar techniques. This leads to a new approach of Fourier domain RDA which is completely equivalent to conventional RDA processing and preserves image integrity. An advantage of this method is that it allows to bypass over-sampling which is dictated by digital implementation of conventional RDA.

The second contribution is a two-dimensional sub-Nyquist SAR system. Relying on Fourier domain RDA and CS, our system enables to sample both range and azimuth axes below the Nyquist rate. Following [21] we begin our development by proposing a one-dimensional sub-Nyquist system for the range axis, which enables low analog-to-digital sampling rates at the receiver. In the preprocessing part, the system exploits the Fourier domain relationship between the signals before and after RCMC in order to generate a subsampled matrix of the corrected signals (following RCMC) from appropriate low-rate raw data samples. The Fourier series coefficients are

extracted from those low-rate samples using Xampling [22], [23]. The Xampling (“compressed sampling”) methodology, uses an architecture that includes an ADC which performs analog prefiltering of the signal before taking point-wise low-rate samples in order to generate sub-Nyquist Fourier coefficients [24]. After preprocessing, CS recovery is applied to reconstruct the image from the partial corrected data.

Next, we propose a system which allows to sample and process the data when fewer pulses are transmitted during a CPI, namely, sub-Nyquist in the azimuth axis. Analogously to the reduced time on target concept applied to radar signals in [25], we propose to exploit the time periods where no pulses are transmitted, to transmit pulses to another zone, using electronic beam steering. This way, we can capture several scenes during the same CPI. This system also supports concurrent subsampling for both axes. However, when one is interested only in range subsampling the first system has faster run time.

In both systems, the sparse recovery algorithm is treated without the use of vectorization, by exploiting the natural two-dimensional structure of SAR data. The core of the method is based on the fast iterative shrinkage thresholding algorithm (FISTA) [26], which allows to handle practical limitations of real SAR data. Using various sparsifying transforms, simulations provided in Section VI show that following reduction of 24% of the Nyquist samples in range, our sub-Nyquist sampling and recovery methods preserve classic RDA processing quality. Moreover, a reduction of more than 50% of the transmitted pulses is presented via simulation for the azimuth axis sub-Nyquist sampling. Simultaneous two-dimensional sub-Nyquist sampling is applied on real SAR data of RADARSAT-1 satellite, leading to a total reduction of about 49% of the original samples processed by conventional systems.

To examine our system we conclude by presenting an experiment of our SAR receiver hardware prototype. We integrated our method into a stand-alone system, using National Instrument (NI) hardware. The system receives SAR returns, samples them at a low-rate and performs our CS recovery. This shows that such processing is feasible in practice.

The remainder of this paper is organized as follows: In Section II we describe the SAR model, the assumptions we use for its simplification and review the classic Range-Doppler algorithm. In Section III we introduce the Fourier domain Range-Doppler algorithm. Our sub-Nyquist method using Fourier domain RDA is described in Section IV, along with an analysis of noiseless recovery. In Section V we show how an image can be reconstructed after dropping some of the transmitted pulses. Simulation results on simulated and real data are presented in Section VI. Finally, in Section VII our approach is implemented on a hardware system showing that it can cope with practical limitations of real radar imaging problems.

II. SAR MODEL AND THE RANGE-DOPPLER ALGORITHM

SAR spaceborne and airborne systems are based on a radar which travels along a well defined path with velocity

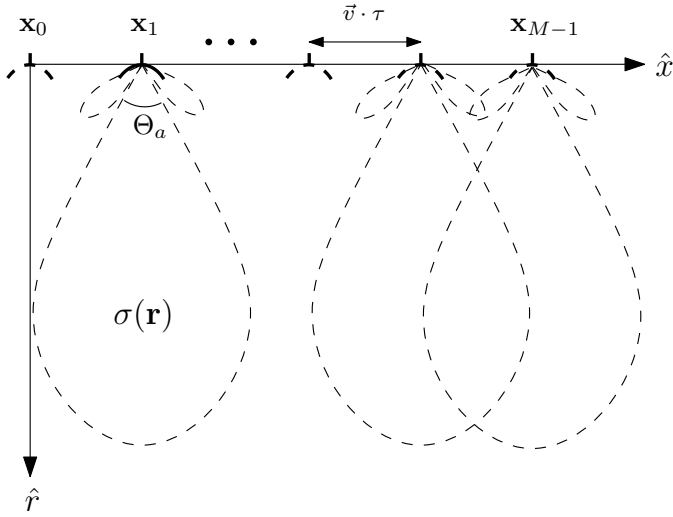


Fig. 1. SAR system model for the stripmap mode. The coherent information is recorded at different positions, spaced by a displacement of $\vec{v}\tau$. At every position the radar, which has an angular aperture of Θ_a , captures a part of the scene reflectivity, $\sigma(\mathbf{r})$.

\vec{v} and transmits every PRI, T , a time-limited pulse $h(t)$ with negligible energy at frequencies beyond $B_h/2$. The transmitted pulses are sent from M different locations, $\{\mathbf{x}_m\}_{m=0}^{M-1}$, where \mathbf{x}_0 is the origin and $\|\mathbf{x}_m - \mathbf{x}_0\| = m|\vec{v}|T$ is the platform displacement at the m th location. The pulses are transmitted into a scene with a stationary terrain reflectivity, $\sigma(\mathbf{r})$, where $\mathbf{r} = (x, r)$ is the scene spatial vector consisting of azimuth and range axes, respectively.

The pulse $h(t)$ is modulated by a pure tone with carrier frequency f_c , so that the transmitted signal is $h(t)e^{j2\pi f_c t}$. The received signal from the m th transmitted pulse, after coherent demodulation, is given by

$$d_m(t) = \int \sigma(\mathbf{r})h(t - 2\|\mathbf{r} - \mathbf{x}_m\|/c)w_a(\mathbf{x}_m, \mathbf{r}) \times (1) \\ e^{-j4\pi f_c \|\mathbf{r} - \mathbf{x}_m\|/c} d\mathbf{r},$$

where $\|\mathbf{r} - \mathbf{x}_m\|$ is the distance from the radar at position \mathbf{x}_m to a scatter point at position \mathbf{r} (no sensor movement is assumed between transmission and reception of a pulse – the “Stop-and-hop” assumption) and $w_a(\mathbf{x}_m, \mathbf{r})$ is the antenna beam pattern. The beam generally forms a spatial squared sinc function with an angular aperture (main lobe) of Θ_a that is inversely proportional to the antenna length. Its steering direction varies depending on the SAR operation mode (stripmap, spotlight, scan SAR, etc.), which are mainly distinguished by resolution and coverage capabilities [4]. For the stripmap mode, the beam pattern is

$$w_a(\mathbf{x}_m, \mathbf{r}) = \text{sinc}^2\left(\frac{|x - x_m|}{r} \cot \frac{\Theta_a}{2}\right), \quad (2)$$

where x_m denotes the azimuth coordinate, \hat{x} , of \mathbf{x}_m . A SAR system model, for the stripmap mode, is depicted in Fig. 1. In practice, $d_m(t)$ will be contaminated by additive white Gaussian noise.

The goal of SAR imaging is to reconstruct the complex scene reflectivity, $\sigma(\mathbf{r})$, from the raw data returns in (1).

In order to perform processing, the analog signals are first sampled. According to the Nyquist theorem, $d_m(t)$ should be sampled at least at B_h , creating $d[n, m] = d_m(nT_s)$, with $0 \leq n < N = \lceil T f_s \rceil$, where $f_s = 1/T_s$ is the sampling rate at the receiver.

After sampling the data is processed. Since the SAR acquisition system is not space-invariant, various algorithms have been developed in order to approximate the reflectivity $\mathbf{I} \approx \sigma(\mathbf{r})$ and to accelerate processing time [2], [3]. RDA is the most common approach and has one of the best accuracy/generality/efficiency tradeoffs among existing algorithms [4].

There are three main steps in implementing RDA:

- 1) Range compression.
- 2) Range cell migration correction.
- 3) Azimuth compression.

In our derivation we use the “low squint angle” assumption, namely, the angle that the transmission is offset from the normal of the plane of the antenna is assumed to be small. This means that a secondary range compression is not required in the processing flow [4].

The range compression stage uses the pulse compression property which states that $h(t) * h^*(-t) = \delta(t)$, where $\delta(t)$ is a narrow pulse with width $1/B_h$. The raw data $d[n, m]$ is therefore compressed in the range direction to

$$\tilde{d}[n, m] = d[n, m] * h^*[-n]. \quad (3)$$

Next, the raw data is transformed to the range-Doppler domain via the discrete Fourier transform (DFT) along the azimuth axis:

$$S[n, k] = \text{DFT}_m \left\{ \tilde{d}[n, m] \right\} = \sum_{m=0}^{M-1} \tilde{d}[n, m] e^{-j2\pi km/M}, \quad (4)$$

followed by RCMC. The purpose of RCMC is to compensate for the effect of range cell migration which were migrated from their origin due to the varied satellite-scatterer distance and to correct the hyperbolic behavior of the target trajectories.

Due to the “low squint angle” assumption, the far field approximation can be applied so that the RCMC operator can be written as

$$C[n, k] = S[n + n \cdot ak^2, k]. \quad (5)$$

For every Doppler frequency k , the range axis is scaled by $1 + ak^2$. In stripmap mode we have, for example, $a = \frac{\lambda^2}{8|\vec{v}|^2 T^2 M^2}$. As can be seen in (5), this range-variant shift requires values which fall outside the discrete grid. There are two ways to implement RCMC: In the first option, RCMC is performed by range interpolation in the Range-Doppler domain. However, this interpolation is time-consuming and computationally demanding. The second approach involves the assumption that the range cell migration is range invariant, at least over a finite range block. In this case, RCMC is implemented using an FFT, linear phase multiply, and IFFT per block. However, this implementation has the disadvantage that blocks have to overlap in range, and the efficiency gain may not be worth the added complexity.

Following RCMC, the signal is compressed in the azimuth direction. The “low squint angle” assumption enables the compression by using a matched filter of a chirp (a.k.a Linear Frequency Modulation) [4]:

$$Y[n, k] = C[n, k]e^{-j\pi \frac{k^2}{K_a[n]}}, \quad (6)$$

where $K_a[n]$ is the range dependent azimuth chirp rate

$$K_a[n] = \frac{4M^2T^2|\bar{v}|^2}{\lambda cnT_S}. \quad (7)$$

An IDFT in the azimuth direction results in the focused data:

$$I[n, m] = \text{IDFT}_k \{Y[n, k]\} = \frac{1}{M} \sum_{k=0}^{M-1} Y[n, k]e^{j2\pi mk/M}. \quad (8)$$

Figure 2 depicts the RDA stages for equally spaced single-point reflectors.

RDA is the preferred algorithm in most SAR operations thanks to its high precision and generality. However, the increase in processing due to the extra interpolation is its main disadvantage. It is evident that processing in the time domain imposes a high sampling rate and considerable burden on the RCMC block. We next show that the number of samples can be reduced significantly by exploiting ideas of processing in the Fourier domain, sub-Nyquist sampling and CS-based signal reconstruction.

III. RANGE DOPPLER ALGORITHM VIA FOURIER COEFFICIENTS

In this section we show that RDA can be performed in frequency, using the Fourier series coefficients of the raw data, paving the way to substantial reduction in the number of samples needed to obtain the same image quality. In particular, we adapt the idea of compressed beamforming in ultrasound imaging [19], [20], to perform RCMC using Fourier series coefficients instead of the expensive time-domain interpolation without any assumptions on the signal structure or the invariance of range blocks. This allows to transfer the process of RDA to the frequency domain, and eliminate the need for over-sampling.

A. Fourier Domain RCMC

Similarly to [20] we begin by calculating the Fourier series coefficients of the continuous version of (5)

$$C_k(t) = S_k(t(1 + ak^2)), \quad (9)$$

where $S_k(nT_s) = S[n, k]$. Denote the Fourier series coefficients of $C_k(t)$ with respect to the interval $[0, T]$ by

$$C_k[l] = \frac{1}{T} \int_0^T I_{[0, T_k]}(t) C_k(t) e^{-i\frac{2\pi}{T}lt} dt, \quad (10)$$

where $T_k = T/(1 + ak^2)$ and $I_{[a, b]}$ is the indicator function which equals 1 when $a \leq t < b$ and 0 otherwise. Substituting (9) into (10) we get

$$C_k[l] = \frac{1}{T} \int_0^T S_k(t) q_{k,l}(t) dt, \quad (11)$$

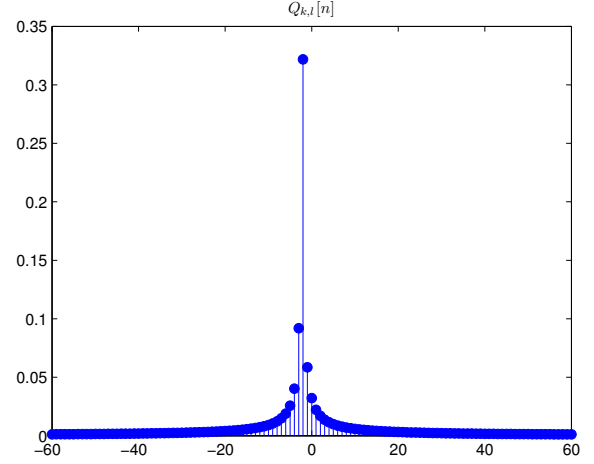


Fig. 3. The Fourier series coefficients $\{Q_{k,l}[n]\}$ of $q_{k,l}(t)$ are characterized by a rapid decay, where most of the energy is concentrated around $n_{k,l}$. Here $k = 4$, $l = 4$ and $a = 2$, so that $n_{k,l} = -2$.

with

$$q_{k,l}(t) = I_{[0, T]}(t) \frac{1}{1 + ak^2} \exp \left\{ -i\frac{2\pi}{T}lt \left(\frac{1}{1 + ak^2} \right) \right\}. \quad (12)$$

We next express $S_k(t)$ in terms of its Fourier series coefficients representation

$$S_k(t) = \sum_{n=-\infty}^{\infty} S_k[n] e^{i\frac{2\pi}{T}nt}. \quad (13)$$

Substituting into (11) leads to

$$\begin{aligned} C_k[l] &= \frac{1}{T} \int_0^T \sum_{n=-\infty}^{\infty} S_k[n] e^{i\frac{2\pi}{T}nt} q_{k,l}(t) dt \\ &= \sum_{n=-\infty}^{\infty} S_k[n] \frac{1}{T} \int_0^T q_{k,l}(t) e^{-i\frac{2\pi}{T}(-n)t} dt \\ &= \sum_{n=-\infty}^{\infty} S_k[n] Q_{k,l}[-n], \end{aligned} \quad (14)$$

where $Q_{k,l}[n]$ are the Fourier series coefficients of $q_{k,l}(t)$. Using the relationship between the continuous time Fourier transform (CTFT) $X(\omega)$ and the Fourier series coefficients $C[l]$ of a finite supported function $x(t)$, $C[l] = \frac{1}{T} X\left(\frac{2\pi}{T}l\right)$, we get

$$Q_{k,l}[n] = \frac{1}{1 + ak^2} e^{-j\pi\left(n + \frac{l}{1 + ak^2}\right)} \text{sinc} \left(n + \frac{l}{1 + ak^2} \right). \quad (15)$$

It is easy to see that most of the energy of the set $Q_{k,l}[n]$ is concentrated around a specific component, $n_{k,l} = \text{round}\left(-\frac{l}{1 + ak^2}\right)$, where the $\text{round}(\cdot)$ operation rounds the argument to its closest integer. This behavior is typical to any choice of k or l . An example with $k = 4$, $l = 4$ and $a = 2$ is shown in Fig. 3. Thus, for every Doppler frequency k , the Fourier series coefficients of the scaled signal, $C_k(t)$, can be calculated as a linear combination (weighted sum) of a local

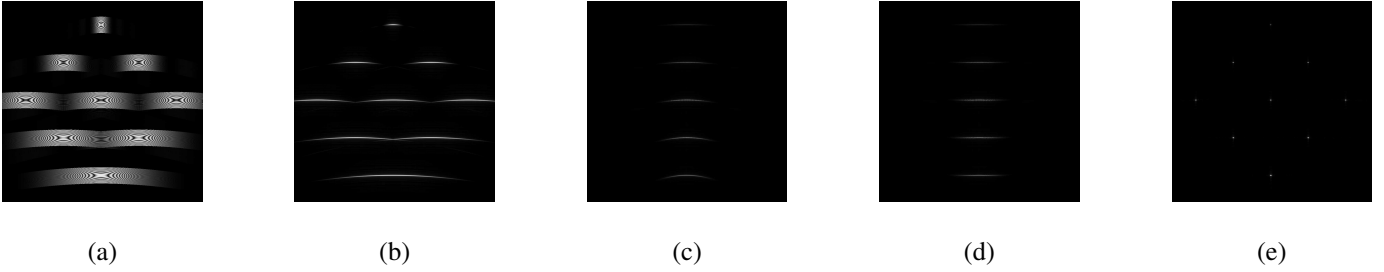


Fig. 2. The Range-Doppler Algorithm (RDA) stages for equally spaced single-point reflectors. (a) Raw data (real component). (b) Range compression. (c) Azimuth DFT. (d) Range cell migration correction (RCMC). (e) Compressed image.

choice of Fourier series coefficients of $S_k(t)$,

$$C_k[l] = \sum_{n \in \nu(k,l)} S_k[n] Q_{k,l}[-n], \quad (16)$$

where $\nu(k,l)$ is the set of indices which is dictated by the decay property of (15).

We conclude that given $S_k[l]$, (16) provides the Fourier series coefficients, $C_k[l]$, of the corrected signal $C_k(t)$ defined in (9).

B. Acquisition in Fourier Domain

Assuming that the samples can be extracted directly in the Fourier domain, the samples are defined via

$$D_m[l] = \frac{1}{T} \int_0^T d_m(t) e^{-i \frac{2\pi}{T} lt} dt. \quad (17)$$

We next show how the preliminary stages of RDA can be performed in the Fourier domain as well.

Range compression can be simply applied in the Fourier domain by

$$\tilde{D}_m[l] = T \cdot D_m[l] H^*[l], \quad (18)$$

where $H[l]$ is the l th Fourier series coefficient of the transmitted pulse, $h(t)$. Next, we perform azimuth DFT on the range Fourier samples

$$S_k[l] = \text{DFT}_m \left\{ \tilde{D}_m[l] \right\} = \sum_{m=0}^{M-1} \tilde{D}_m[l] e^{-i 2\pi km/M}. \quad (19)$$

For every Doppler frequency we then use (16) to apply RCMC and calculate the (range) scaled signal Fourier series coefficients. Applying an inverse Fourier transform on $\{C_k[l]\}$ reconstructs the corrected sampled signal after RCMC,

$$C[n, k] = \sum_{l=-\infty}^{\infty} C_k[l] e^{i \frac{2\pi}{T} lnT_s}. \quad (20)$$

We then continue to the original procedure by applying (6) and (8) to complete the processing. A comparison between Fourier domain RDA and conventional RDA is introduced in Table I.

C. Sampling and processing at the Nyquist rate

In practice, SAR signals are sampled at rates which are higher than the Nyquist rate. A typical over-sampling factor of 1.5 to 4 times the transmitted signal bandwidth allows to increase the accuracy of the digital interpolation in the RCMC stage and eliminate artifacts caused by digital implementation of standard RDA processing. While achieving the same results, we next show how our algorithm can be performed without over-sampling.

Denote by β_m , $|\beta_m| = B$, the set of Fourier series coefficients of the detected signal, $d_m(t)$, that correspond to its bandwidth, namely, the values of l for which $D_m[l]$ is nonzero (or larger than a threshold). The ratio between the cardinality of the set β_m and the overall number of samples $N = \lfloor T f_s \rfloor$, required by standard RDA is dictated by the oversampling factor.

The bandwidth of the returned signals in (1) is equal to the bandwidth of the transmitted signal, $H[l]$. Thus, following range compression in (18), the bandwidth of the signals remains the same. Moreover, it is easy to see that the azimuth DFT stage in (19) preserves the bandwidth of the range compressed signal, and that for every Doppler frequency k , the cardinality of the non-zero $\{S_k[l]\}$ equals to B . However, (16) implies that the bandwidth of the corrected signals following RCMC, β_k , will contain at most $B + |\nu(k,l)|$ nonzero frequency components. Due to the azimuth DFT operation, to compute the elements in β_k all we need is the set β_m from each one of the detected signals. In a typical imaging setup B is on the order of thousands of coefficients, while $\nu(k,l)$, defined by the decaying properties of $\{Q_{k,l}[n]\}$, is typically no larger than 10. This implies that $B \gg |\nu(k,l)|$, so $|\beta_k| = B + |\nu(k,l)| \approx B$. Hence, the bandwidth of the corrected signals is approximately equal to the bandwidth of the detected signals, which means that sampling and processing can be done at the Nyquist rate and no over-sampling is required. In a typical system setup this reduction leads to $B/N = 2/3$ to $1/4$. Figure. 4 depicts the Fourier series coefficients which are taken within the effective bandwidth.

D. Simulation and validation

To demonstrate the equivalence of RDA in time and frequency, we applied both methods on simulated SAR raw data.

First, we evaluate the required number of $|\nu(k,l)|$ by measuring the reconstruction quality via the peak sidelobe ratio (PSLR) of the point spread function (PSF) of the system.

| Algorithm stage | Range-Doppler Algorithm | Fourier domain RDA |
|---------------------|---|--|
| Range compression | $\tilde{d}[n, m] = d[n, m] * h^*[-n]$ | $\tilde{D}_m[l] = T \cdot D_m[l] H^*[l]$ |
| Azimuth DFT | $S[n, k] = \sum_{m=0}^{M-1} \tilde{d}[n, m] e^{-j2\pi km/M}$ | $S_k[l] = \sum_{m=0}^{M-1} \tilde{D}_m[l] e^{-j2\pi km/M}$ |
| RCMC | $C[n, k] = S[n + n \cdot ak^2, k]$ | $C_k[l] = \sum_{n \in \nu(k,l)} S_k[n] Q_{k,l}[-n]$ |
| Azimuth compression | $Y[n, k] = C[n, k] e^{-j\pi \frac{k^2}{K_a[n]}}$ | $Y[n, k] = \left(\sum_{l \in \beta_k} C_k[l] e^{i \frac{2\pi}{T} l n T_s} \right) e^{-j\pi \frac{k^2}{K_a[n]}}$ |
| Azimuth IDFT | $I[n, m] = \frac{1}{M} \sum_{k=0}^{M-1} Y[n, k] e^{j2\pi mk/M}$ | $I[n, m] = \frac{1}{M} \sum_{k=0}^{M-1} Y[n, k] e^{j2\pi mk/M}$ |

TABLE I
FOURIER DOMAIN RDA COMPARED TO CONVENTIONAL RDA

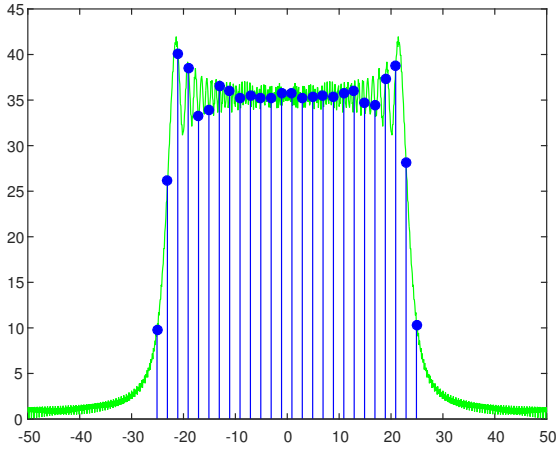


Fig. 4. Fourier series coefficients are taken within the effective bandwidth of the returned signals. Since the signals are finite in time the coherent information within the discrete frequency samples is sufficient to handle SAR processing.

Assuming that no windowing is applied to the range and azimuth signals, the PSF can be approximately described as a two-dimensional sinc function, and its beam widths in range and azimuth are inversely proportional to the transmitted signal bandwidth and the Doppler bandwidth, respectively. PSLR is defined as the ratio of the peak intensity of the most prominent sidelobe to the peak intensity of the main lobe, i.e., the smaller the PSLR, the better an image quality.

The PSF was generated by a single reflector in the scene center as the input of the system, $\sigma(\mathbf{r}) = \delta(\mathbf{r} - \mathbf{r}_c)$. Results are shown in Fig. 5. It can be seen that $|\nu(k, l)| = 5$ components of each $S_k[n]$ are sufficient to achieve almost the same quality, visually and quantitatively.

In addition, we examined the equivalence of both methods on SAR raw data which was simulated from a real SAR image as a reflectivity map, $\sigma(\mathbf{r})$. To verify the selection of $|\nu(k, l)|$ we compare the resulting image of time RDA processing with Fourier domain RDA using a varied number of $|\nu(k, l)|$. We measured the similarity using a state of the art image quality

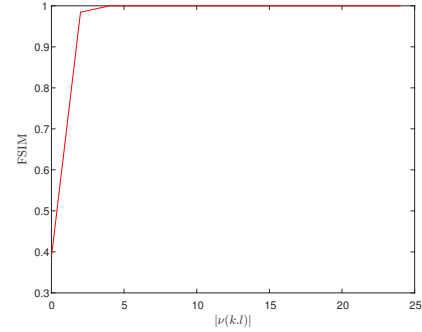


Fig. 6. Similarity between the conventional RDA and the Fourier domain RDA for a varied number of $|\nu(k, l)|$ using FSIM.

assessment index call FSIM [27]. From Fig. 6 it is readily seen that the effect of considering more than 5 coefficients is negligible. The parameters of the system are described in Table II. The ratio between the cardinality of the set β_m and the overall number of samples N , required by standard RDA rate f_s , is dictated by the oversampling factor, α_{os} . Since $f_s = \alpha_{os} N$, the new rate leads to a reduction of $B/N = \frac{1}{2}$. Figure 7(a) shows the image follows time RDA processing while in Fig. 7(b) we use Fourier RDA processing with $|\nu(k, l)| = 5$. As can be readily seen, the images look identical. These results verify that both signals and the resulting images are extremely similar.

To conclude this section, we presented a new algorithm, equivalent to RDA, that instead of time interpolation, can correct the migration of range cells in the Fourier domain. We exploited the effective bandwidth of SAR signals and bypassed oversampling, dictated by digital implementation of RCMC in time without any over sampling factor, assumption on the signal structure or the invariance of range blocks.

IV. SUBSAMPLING IN FAST TIME

In this section, we demonstrate how RDA in frequency allows for sub-Nyquist sampling of the individual received signals when exploiting sparsity of SAR images.

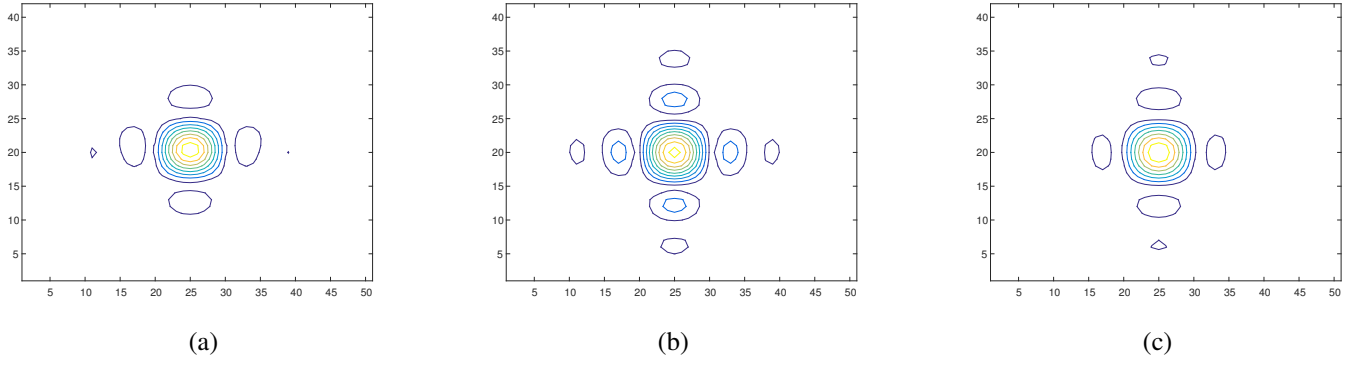
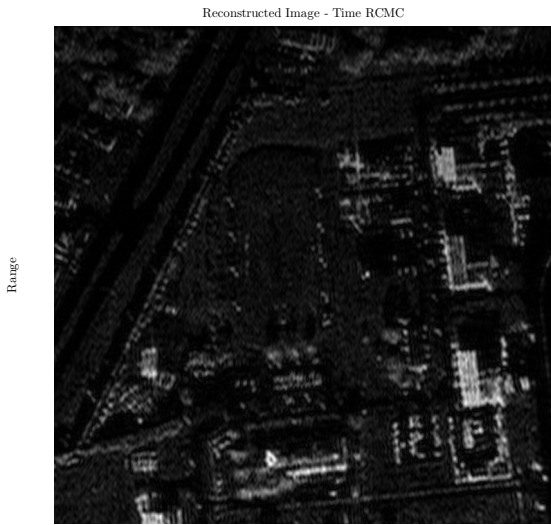
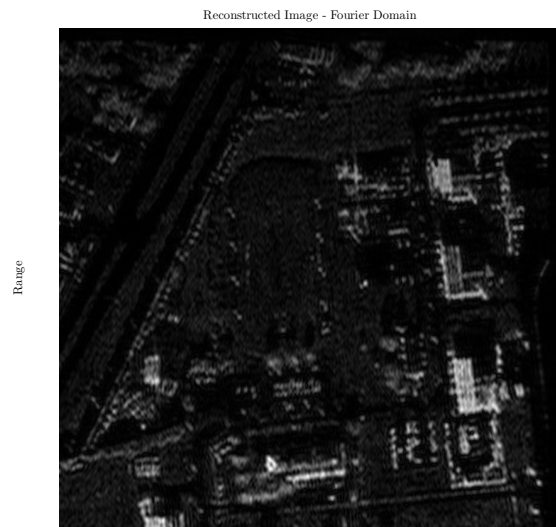


Fig. 5. A point spread function (PSF) of a SAR system simulated with different RDA techniques. (a) Conventional RDA, PSLR = 13.32 [dB]. (b) Fourier domain RDA, $|\nu(k, l)| = 3$, PSLR = 11.7598 [dB]. (c) Fourier domain RDA, $|\nu(k, l)| = 5$, PSLR = 13.29 [dB].



(a)



(b)

Fig. 7. Comparison of reconstructed image: (a) Conventional RDA. (b) Fourier RDA, $|\nu(k, l)| = 5$.

A. Rate reduction via compressed sensing

Denote by $\mathbf{C} = \{C_k[l]\}_{0 \leq k < M}^{l \in \beta_k} \in \mathbb{C}^{B \times M}$ the partial Fourier coefficients matrix of the corrected signals in (16).

Having \mathbf{C} , and using the processing stages in (6), (8), and (20), the relationship between the image and the processed Fourier coefficients can be formulated as

$$\mathbf{C} = \mathbf{F}^s [\mathbf{B} \circ (\mathbf{I}\mathbf{F})], \quad (21)$$

where $\mathbf{F}^s = \left\{ \frac{1}{B} e^{-j \frac{2\pi}{B} lk} \right\} \in \mathbb{C}^{B \times N}$ is a partial DFT matrix, $\mathbf{B} = \left\{ e^{j\pi \frac{k^2}{K_a[n]}} \right\} \in \mathbb{C}^{N \times M}$ is the azimuth compression matrix from (6), $\mathbf{F} \in \mathbb{C}^{M \times M}$ is the DFT matrix, \circ is the Hadamard product and $\mathbf{I} = \{I[n, m]\} \in \mathbb{C}^{N \times M}$ is the desired image.

When there exist a basis in which \mathbf{I} is sparsely represented, (21) becomes a sparse recovery problem which can be solved using a subset of the rows of \mathbf{C} , namely, a smaller number of Fourier coefficients of each of the corrected signals. A typical formulation for the optimization problem is:

$$\min \|\Psi(\mathbf{I})\|_1 \quad \text{s.t.} \quad \|\mathbf{C}_p - \mathbf{F}_p^s [\mathbf{B} \circ (\mathbf{I}\mathbf{F})]\|_F^2 < \epsilon, \quad (22)$$

where \mathbf{C}_p and \mathbf{F}_p^s are row undersampled versions of \mathbf{C} and \mathbf{F}^s , Ψ is a sparsifying transform operator, $\|\cdot\|_F$ is the Frobenius norm and ϵ controls the fidelity of the reconstruction to the measured data.

There are various approaches to solve this optimization problem. One method is to use vectorization:

$$\min \|\Psi(\mathbf{x})\|_1 \quad \text{s.t.} \quad \|\mathbf{y} - \mathbf{M}\mathbf{x}\|_2 \leq \epsilon \quad (23)$$

where $\mathbf{x} = \text{vec}(\mathbf{I})$, $\mathbf{c} = \text{vec}(\mathbf{C})$ and $\mathbf{M} = \bar{\mathbf{F}}^s \bar{\mathbf{B}} \bar{\mathbf{F}}$ with $\bar{\mathbf{F}}^s = \bar{\mathbf{I}} \otimes \mathbf{F}_r^s$, $\bar{\mathbf{B}} = \text{diag}\{\text{vec}(\mathbf{B})\}$ and $\bar{\mathbf{F}} = \mathbf{F}^T \otimes \bar{\mathbf{I}}$, where \otimes is Kronecker product and $\bar{\mathbf{I}}$ is the appropriate unit matrix. A variety of CS techniques can then be employed to solve (23), such as interior point methods [28] and alternating direction method of multipliers (ADMM) [29], [30]. Fast iterative shrinkage-thresholding algorithms such as FISTA [26] or its monotonic version MFISTA [31] are more favorable in dealing with large dimensional data since they do not require structure. However, the original version (22) needs to be updated to handle the natural two-dimensional structure of the problem without using vectorization which increases the dimensions.

B. Exploiting Fourier domain RCMC structure

In order to construct a full sub-Nyquist sampling system, three main questions should be addressed:

- 1) How many Fourier coefficients of the raw data, $D_m[l]$, should be considered in order to extract \mathbf{C}_p ?
- 2) How do we select these Fourier coefficients, considering practical limitations?
- 3) How can these coefficients be achieved in the Fourier domain without full time domain sampling at the Nyquist rate?

We begin by answering the third question. Note that in practice, sampling is performed in time, while our goal is to extract the samples in the Fourier domain. To this end, similarly to [19], we can use the Xampling mechanism. The Xampling philosophy ties together sub-Nyquist sampling based on analog preprocessing with techniques of CS for recovery. However, these approaches typically require sophisticated sampling schemes, which acquire generalized measurements of the analog signals [9], [32]. The authors in [12] presented a concrete analog-to-digital conversion scheme and a recovery algorithm for sampling radar signals at sub-Nyquist rates. The analog input is split into channels, where in each channel it is mixed with the selected harmonic signal, integrated over the PRI duration, and then sampled. The matching Fourier coefficients were then created digitally. This Xampling scheme allows to obtain K coefficients from K point-wise samples of the detected signal filtered with an appropriate kernel $s^*(-t)$, designed according to the transmitted pulse-shape and the chosen set of coefficients.

To answer the first question, we next examine the subset of samples, $\kappa \subset \beta_m$. These coefficients need be extracted from each of the individual returns in order to compute \mathbf{C}_p .

Due to the decay property of (15), the relationship in (16) implies that calculation of a specific Fourier coefficient $C_k[l]$, requires only $|\nu(k, l)|$ coefficients of $\{S_k[l]\}_l$. The decay rate of (15) and thus the cardinality of $\nu(k, l)$ is dictated by the behavior of the sinc function and is independent of k or l . We denote the cardinality of $\nu(k, l)$ by L . Thus, for a given Doppler frequency k , in order to compute an arbitrary set of B coefficients from $\{C_k[l]\}_l$, only $B + L$ coefficients $\{S_k[l]\}_l$ are needed.

Considering the azimuth DFT in (19) it is easy to see that in order to extract a specific coefficient $S_k[l]$ we need the entire set of $\{D_m[l]\}_m$. Therefore, to evaluate an individual coefficient, $C_k[l]$, the indices of the coefficients which should be xampled from each individual signal are $\nu(k, l)$. Generalizing the concept for the entire matrix, in order to extract $\mathbf{C}_p = \{C_k[l]\}_{0 \leq k < M}^{l \in \tilde{\kappa}}$, where $\kappa \subset \beta_k$, only $\mathbf{D}_p = \{D_m[l]\}_{0 \leq m < M}^{l \in \tilde{\kappa}}$ should be xampled, where $\tilde{\kappa} \subset \beta_m$. The preprocessing stage is depicted in Fig. 8.

We next show that κ and $\tilde{\kappa}$ are of the same order of magnitude, which means that the preprocessing stages do not influence the number of required samples.

From the ‘‘low squint angle’’ assumption we have that when the squint angle is low, the range cell migration is relatively small. We may therefore assume that $ak^2 \ll 1$ for every $0 \leq k < M$. To justify this assumption note that for the

stripmap mode $ak^2 = \frac{1}{8} \left(\frac{\lambda}{vT}\right)^2 \left(\frac{k}{M}\right)^2 < \frac{1}{8} \left(\frac{\lambda}{vT}\right)^2$ for every k . In the SEASAT-A satellite [33], $\lambda = 0.235$ [m], $v = 7000$ [m/s], $T = 0.6$ [msec], which yields $\frac{1}{8} \left(\frac{\lambda}{vT}\right)^2 = 3.8 \times 10^{-4}$, justifying the approximation. This assumption means that the most dominant coefficient, $Q_{k,l}[-n]$, is $n_{k,l} \approx l$, a fact which implies that $\nu(k, l)$ is approximately independent of k , and leads to the approximation that the azimuth DFT operation does not influence the number of required samples,

$$|\kappa_m| = \left| \bigcup_{k,l} \nu(k, l) \right| \approx B + L. \quad (24)$$

As was shown in Section III-D, we selected L to be 5. This means that when $B \gg L$, the preprocessing stages do not drastically enlarge the number of required samples.

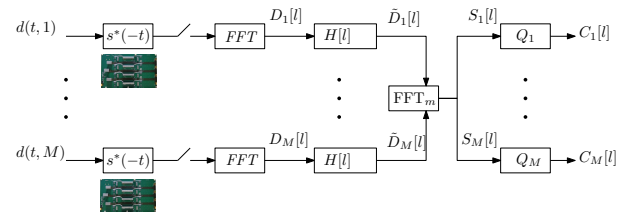


Fig. 8. Preprocessing of sub-Nyquist system using Fourier domain RDA. The raw data is sampled using the xampling prototype in [12], then compressed in range followed by azimuth DFT. The block Q_i represents averaging the DFT coefficients of the detected signals with weights $\{Q_{k,i}[n]\}$ according to (16).

We next address the second question, where the main trade-off is between the selection of consecutive and random coefficients. Unfortunately, random frequency sampling is not practical in hardware. While consecutive coefficients can be obtained using a simple low-pass filter (LPF), it is shown in [19] that a distributed selection results in better recovery and noise robustness. However, implementing an arbitrary choice of isolated frequency samples requires multiple pass-bands and extremely high frequency selectivity. These characteristics are difficult to satisfy when designing a practical analog filter. Some practical guidelines for choosing the frequencies, suggested in [34] to solve the trade-off between noise robustness. Similarly to [12], in our application, we choose a constellation consisting of four groups of coefficients, where the coefficients in each group are consecutive. We refer to this choice as multiple bandpass sampling. The bandpass constellation has the advantage of acquiring the measurements over a wider frequency aperture while it still allows practical hardware implementation. We use a similar sampling scheme in our experiment in Section VII.

C. Fast sparse recovery

In many applications which apply CS on high dimensional data, the reconstruction stage is generally longer than the runtime needed for conventional processing. In the field of SAR, most of the existing CS schemes stack the whole two-dimensional reflectivity map to a vector [15], [17], [35]. This vector is usually very large and leads to a high dimensional sensing matrix. Due to the long reconstruction time and large

memory requirements, it is difficult to reconstruct a moderate-size scene using CS in practice.

We next show how (22) can be solved by extending FISTA [26] to support two-dimensional matrix recovery which fits the SAR problem without the use of vectorization. We apply the same technique as in [36] in order to convert the one-dimensional algorithm to two-dimensional. The proposed algorithm is coined SAR FISTA.

FISTA relies on soft thresholding and gradient decent. The soft operator for a matrix \mathbf{X} is defined via

$$\text{soft}(\mathbf{X}, \alpha) = \frac{\mathbf{X}_{ij}}{|\mathbf{X}_{ij}|} (|\mathbf{X}_{ij}| - \alpha)_+. \quad (25)$$

The Lipschitz constant of $\mathbf{F}(\mathbf{I})$, L_f , controls the gradient decent step of the error function, which equals

$$\mathbf{F}(\mathbf{I}) = \|\mathbf{C} - \mathbf{F}^s[\mathbf{B} \circ (\mathbf{I}\mathbf{F})]\|_{\mathbf{F}}^2. \quad (26)$$

Using matrix differentiation techniques we get the error function gradient

$$\nabla \mathbf{F}(\mathbf{I}) = 2 \left\{ \mathbf{B} \circ \left[\mathbf{F}^{sH}(\mathbf{F}^s(\mathbf{B} \circ (\mathbf{I}\mathbf{F})) - \mathbf{C}) \right] \right\} \mathbf{F}^H \quad (27)$$

where H is the adjoint operator. Algorithm 1 describes the modified version of FISTA which supports the structure of (22).

Algorithm 1 SAR FISTA for sub-Nyquist sampling in range

Input: Samples $\mathbf{D}_p = \{D_m[l]\}_{0 \leq m < M}^{l \in \tilde{\kappa}}$, measurement matrices \mathbf{F}_p^s , \mathbf{B} and \mathbf{F}

Output: estimate for sparse coefficients of SAR image, $\hat{\mathbf{X}}$, such that $\mathbf{I} = \Psi^{-1}(\hat{\mathbf{X}})$

1: **Initialization:** $\mathbf{C}_p = \{C_k[l]\}_{0 \leq k < M}^{l \in \tilde{\kappa}} \leftarrow \mathbf{D}_p$ via (15), (18) and (19)

Initialize: $\mathbf{X}^0 = \mathbf{0}$, $\mathbf{X}^1 = \mathbf{0}$, $t_0 = 1$, $t_1 = 1$, $k = 1$
 $\lambda_1, \beta \in (0, 1)$, $\bar{\lambda} > 0$

2: **while** not converged **do**

3: $\mathbf{Z}^k = \mathbf{X}^k + \frac{t_{k-1}-1}{t_k} (\mathbf{X}^k - \mathbf{X}^{k-1})$

4: $\mathbf{U}^k = \mathbf{Z}^k - \frac{1}{L_f} \nabla \mathbf{F}(\Psi^{-1}(\hat{\mathbf{X}}))$, via (27)

5: $\mathbf{X}^{k+1} = \text{soft}\left(\mathbf{U}^k, \frac{\lambda_k}{L_f}\right)$, via (25)

6: $t_{k+1} = \frac{1 + \sqrt{4t_k^2 + 1}}{2}$

7: $\lambda_{k+1} = \max(\beta \lambda_k, \bar{\lambda})$

8: $k = k + 1$

9: **end while**

$\hat{\mathbf{X}} = \mathbf{X}$

V. REDUCED TIME ON SCENE

In Section IV we proposed an algorithm which exploits sparsity of SAR images in order to reduce sampling rate in the range axis (fast-time). Since SAR can be treated as a two-dimensional sampling problem, we next show how by a few additional derivations the azimuth (slow-time axis) can be subsampled below the Nyquist rate as well.

While an analog to digital converter controls the sampling rate of the received signal at the receiver and is aimed at

preventing aliasing, the need to avoid azimuth ambiguities in the resulting radar image leads to the requirement of dense spatial sampling of the entire scene. More fundamentally, for SAR systems, this dense sampling results in a minimum PRF requirement, which spatially samples the scene every PRI. According to the Nyquist theorem, in order to perfectly reconstruct an image during a CPI, the entire coherent information from the scene should be recorded while the PRF needs to be greater than the Doppler bandwidth of the system, which exists due to the relative velocity between the radar and the ground scatterers. The Doppler bandwidth is equal to product of the azimuth chirp rate in (7) and the time period when the relevant scatterer is exposed to the beam. In the stripmap mode an approximation of the beam pattern in (2) to a time window, leads to a Doppler bandwidth of $2v/l_a$, where l_a is the actual antenna length [4]. This bandwidth, and thus the azimuth resolution, is independent either in range or in the carrier frequency.

We next propose an algorithm which exploits sparsity of SAR images and is aimed at reducing the number of transmitted pulses by sending them non-uniformly, namely, allowing for non-uniform time steps between the pulses while preserving the original CPI. This non-uniform transmission can be interpreted as a *reduced time on scene* concept, which stands for the reduction of time that the radar beam needs to steer at the scatters within the scene. We may exploit the resulting time duration gaps in order to capture more than one scene during the CPI.

A. Azimuth rate reduction via compressed sensing

To develop a CS framework which allows reduction in the number of transmitted pulses, we next derive the inverse RCMC operator in order to isolate the raw data matrix in the CS recovery stage. Relying on sparse properties of the resulting image, this operation enables full image reconstruction with reduced raw data columns, which is equivalent to the omission of transmitted pulses. The inverse operator converts the corrected signals back to their migrated form via Fourier coefficients. This allows to treat RCMC (which is analogous to beamforming in frequency for ultrasound [20]) in the CS recovery stage and not in the preprocessing part.

In order to develop the inverse RCMC operator, we use similar techniques as in Section III-A, to get

$$S_k[l] = \sum_{n \in \tilde{\nu}(k,l)} C_k[n] \tilde{Q}_{k,l}[-n], \quad (28)$$

where

$$\tilde{Q}_{k,l}[n] = (1 + ak^2) e^{-j\pi(n+l(1+ak^2))} \text{sinc}(n + l(1 + ak^2)). \quad (29)$$

Here $C_k[n]$ and $S_k[l]$ are the Fourier series coefficients, after and before RCMC, respectively. For every Doppler frequency k , the Fourier series coefficients of the scaled signal, $S_k(t)$, can be calculated as a linear combination of a local choice of Fourier series coefficients of $C_k(t)$, where $\tilde{\nu}(k, l)$ is the set of indices dictated by the decay property of (29). This decay is identical to the RCMC decay in (15), and therefore we use the results from Section III-D to dictate the cardinality of $\tilde{\nu}(k, l)$.

Having the Fourier coefficients matrix of the range compressed signals, $\tilde{\mathbf{D}} = \{\tilde{D}_m[l]\} \in \mathbb{C}^{B \times M}$, the rest of Fourier domain RDA processing can be formulated as

$$\tilde{\mathbf{D}} = \tilde{\mathbf{Q}}(\mathbf{F}^s [\mathbf{B} \circ (\mathbf{I}\mathbf{F})]) \mathbf{F}^*, \quad (30)$$

where $\tilde{\mathbf{Q}}(\cdot)$ represents the inverse RCMC operator, $\mathbf{S} = \tilde{\mathbf{Q}}(\mathbf{C})$, which is defined via (28).

Similarly to Section IV-A, when there exists some basis in which \mathbf{I} can be sparsely represented, (30) becomes a CS problem that can be solved using a smaller amount of columns in $\tilde{\mathbf{D}}$. Since each column represents the echoes from a specific pulse, solving the problem with reduced number of columns enables to reconstruct the scene while dropping some of the pulses. The resulting optimization problem is:

$$\min \|\Psi(\mathbf{I})\|_1 \quad \text{s.t.} \quad \left\| \tilde{\mathbf{D}}_p - \tilde{\mathbf{Q}}(\mathbf{F}^s [\mathbf{B} \circ (\mathbf{I}\mathbf{F})]) \mathbf{F}_p^* \right\|_F^2 < \epsilon \quad (31)$$

where $\tilde{\mathbf{D}}_p$ and \mathbf{F}_p^* are column under-sampled version of $\tilde{\mathbf{D}}$ and \mathbf{F}^* , respectively. These missing columns represent the omitted pulses. We denote the subsampled set of columns by \tilde{M} . Similarly to Section IV-A, due to the linearity of the operators, (31) can be solved using vectorization. However, here as well, FISTA may be extended using the gradient of the error function:

$$\mathbf{G}(\mathbf{I}) = \left\| \tilde{\mathbf{D}}_p - \tilde{\mathbf{Q}}(\mathbf{F}^s [\mathbf{B} \circ (\mathbf{I}\mathbf{F})]) \mathbf{F}_p^* \right\|_F^2, \quad (32)$$

which equals to

$$\nabla \mathbf{G}(\mathbf{I}) = 2 \left\{ \mathbf{B} \circ \left[\mathbf{F}^{sH} \tilde{\mathbf{Q}}^H (\mathbf{E}\mathbf{F}_p^T) \right] \right\} \mathbf{F}^H, \quad (33)$$

where

$$\mathbf{E} = \tilde{\mathbf{D}}_p - \tilde{\mathbf{Q}}(\mathbf{F}^s [\mathbf{B} \circ (\mathbf{I}\mathbf{F})]) \mathbf{F}_p^*. \quad (34)$$

Unlike Algorithm 1, here the preprocessing stages include only range compression via (18).

Similarly to the reduced-time on target concept which is introduced in [25], the columns of $\tilde{\mathbf{D}}_p$ are selected randomly.

Our steps for azimuth subsampling are summarized in Algorithm 2.

B. Time gaps exploitation

Non-uniform pulse transmission results in time gaps within the CPI where no echoes are recorded. Similarly to [25], which uses the same concept for radar signals, we propose to exploit these time gaps, for sending pulses to other scenes. This allows to capture several different scenes within the same CPI and therefore using the same size of memory to form several images instead of one. This memory reduction has significant meaning in orbital missions which are limited by on-board memory and downlink throughput. The processing of each image is performed separately, since every scene is processed with its own partial Fourier IDFT matrix, \mathbf{F}_p^* in (31), with the indices of the relevant pulses.

Although these time gaps are on the order of milliseconds, phased array and electronic beam-steering techniques can aim the beam to different directions within those time periods, by controlling the phased array parameters [37]. In the simulations, we show that two different scenes can be captured during

Algorithm 2 SAR FISTA for sub-Nyquist sampling in azimuth

Input: SAR raw data samples $\mathbf{D}_p = \{D_m[l]\}_{m \in \tilde{M}}^{l \in \tilde{\kappa}}$, measurement matrices $\mathbf{F}_p^s, \mathbf{B}, \mathbf{F}$

Output: estimate for sparse coefficients of SAR image, $\hat{\mathbf{X}}$, such that $\mathbf{I} = \Psi^{-1}(\hat{\mathbf{X}})$

- 1: **Initialization:** $\tilde{\mathbf{D}}_p = \{\tilde{D}_m[l]\}_{m \in \tilde{M}}^{l \in \tilde{\kappa}} \leftarrow \mathbf{D}_p$ via (18)
- Initialize:** $\mathbf{X}^0 = \mathbf{0}, \mathbf{X}^1 = \mathbf{0}, t_0 = 1, t_1 = 1, k = 1$
 $\lambda_1, \beta \in (0, 1), \bar{\lambda} > 0$
- 2: **while** not converged **do**
- 3: $\mathbf{Z}^k = \mathbf{X}^k + \frac{t_k - 1}{t_k} (\mathbf{X}^k - \mathbf{X}^{k-1})$
- 4: $\mathbf{U}^k = \mathbf{Z}^k - \frac{1}{L_f} \nabla \mathbf{G}(\Psi^{-1}(\hat{\mathbf{X}}))$, via (33)
- 5: $\mathbf{X}^{k+1} = \text{soft}\left(\mathbf{U}^k, \frac{\lambda_k}{L_f}\right)$
- 6: $t_{k+1} = \frac{1 + \sqrt{4t_k^2 + 1}}{2}$
- 7: $\lambda_{k+1} = \max(\beta \lambda_k, \bar{\lambda})$
- 8: $k = k + 1$
- 9: **end while**

$\hat{\mathbf{X}} = \mathbf{X}$

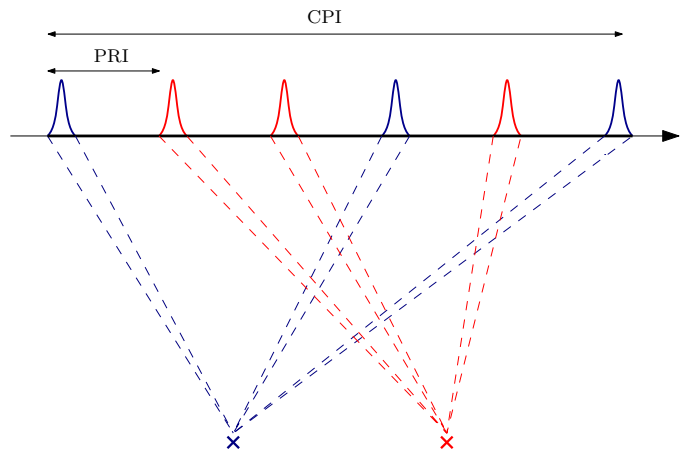


Fig. 9. Reduced time on scene. The transmitted pulses are non-uniformly sub-sampled. The complementary pulses are exploited to capture another scene.

a single CPI. Figure 9 depicts the reduced time on scene and time gaps exploitation concept.

C. Two-dimensional sub-Nyquist sampling

Algorithm 2 can be used to perform range subsampling concurrent to pulses omission. This results in a two-dimensional sub-Nyquist SAR system.

The corresponding optimization problem is formulated via:

$$\min \|\Psi(\mathbf{I})\|_1 \quad \text{s.t.} \quad \left\| \tilde{\mathbf{D}}_{pp} - \tilde{\mathbf{Q}}_p(\mathbf{F}^s [\mathbf{B} \circ (\mathbf{I}\mathbf{F}_a)]) \mathbf{F}_p^* \right\|_F^2 < \epsilon \quad (35)$$

where $\tilde{\mathbf{D}}_{pp}$ is both column and row under-sampled version of $\tilde{\mathbf{D}}$ and $\tilde{\mathbf{Q}}_p(\cdot)$ is the partial RCMC operator which counts only the $l \in \tilde{\kappa}$ Fourier coefficients.

The recovery algorithm of (35) is similar to Algorithm 2 when $\tilde{\mathbf{D}}_p$ and $\tilde{\mathbf{Q}}$ are replaced by $\tilde{\mathbf{D}}_{pp}$ and $\tilde{\mathbf{Q}}_p$, respectively. In case we consider runtime, the expensive three-dimensional linear operation of Fourier RCMC (28), which takes place

at every iteration when calculating the gradient step in the recovery stage, dictates the runtime of Algorithm 2. However, in Algorithm 1 we use this operation only once at the initialization stage in calculating C_p . For that reason, if we only want to subsample in azimuth, then Algorithm 1 is preferred.

VI. SIMULATIONS

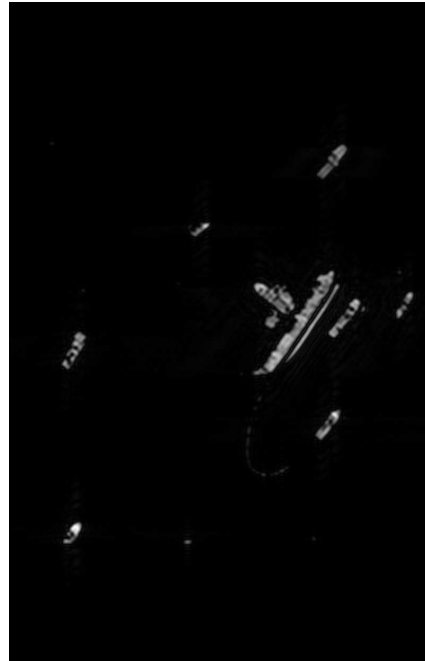
In this section, we examine the performance of Fourier domain RDA sub-Nyquist sampling and recovery for both range and azimuth axes. We compare the methods to the conventional RDA approach with full Nyquist samples. This is done by applying both methods to simulated and real SAR data, using various kinds of sparsity.

A. Simulated Data

In order to examine our methods, we generated SAR raw data of two different scenes: a spatially sparse scene and a scene which is sparse under the Daubechies-4 wavelet basis. The data was generated from real SAR images, using the model in (1) where the reflectivity map was taken as the original image, namely, each pixel in the image is treated as a point reflector, $\sigma(\mathbf{r}) = I(\mathbf{r})$.

The first scene in the image includes sea with several vessels. Since there is nearly no back reflection from the water surface, large areas in the scene have almost no reflectivity, namely, this image is spatially sparse. The number of transmitted pulses is $P = 1200$ and the rest of the system parameters are described in Table II. We processed the image using only 120 Fourier coefficients from each received signal, instead of the $F_s T = 500$ which are required in order to satisfy RDA with $\alpha_{os} = 2$. We compared the conventional Range-Doppler processing with full samples, to Algorithm 1. The algorithm parameters are: $\beta = 0.9, \lambda = 1000, \bar{\lambda} = 1000, L_f = 1$ and Ψ is taken as the unit transform. Figure 10 (a) depicts the scene processed with conventional RDA. Figure 10 (b) depicts the results of our sub-Nyquist sampling and processing approach using Algorithm 1. It is seen that our CS algorithm outperforms the conventional RDA with only 24% of the coefficients required in conventional RDA. We may note that for spatially sparse scene the reconstructed image is sharper. SAR FISTA has sharpened the image due to the attenuation of PSF side lobes caused by the soft thresholding operation (25).

In the next simulation we examine the azimuth rate reduction. The scene in the image includes two islands. In this case it is easy to see that the image is not spatially sparse. Thus, we used the Daubechies-4 wavelet transform as the sparsifying basis. The number of transmitted pulses is $P = 1200$ and the rest of the system parameters remain the same. The PRF here is dictated by the Nyquist theorem and should be higher than 25 KHz for $l_a = 6$ m. We processed the data with Algorithm 2 using only 600 pulses instead of 1200. We compared the conventional Range-Doppler processing with full pulses transmission. The algorithm parameters are: $\beta = 0.8, \lambda = 800, \bar{\lambda} = 800, L_f = 1$. The results are shown in Fig. 11. It can be seen that our CS algorithm achieves results which are equivalent to the conventional RDA with only 50%

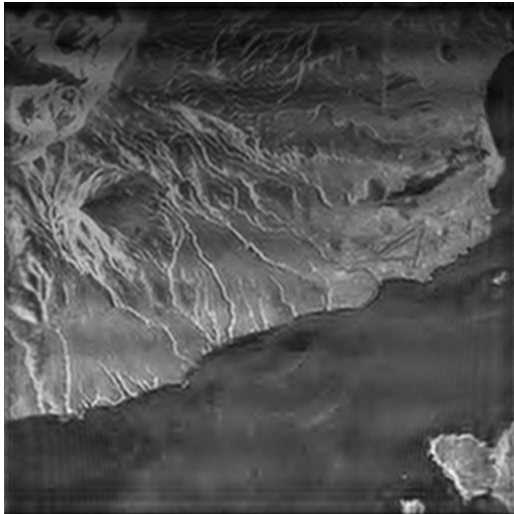


(a)

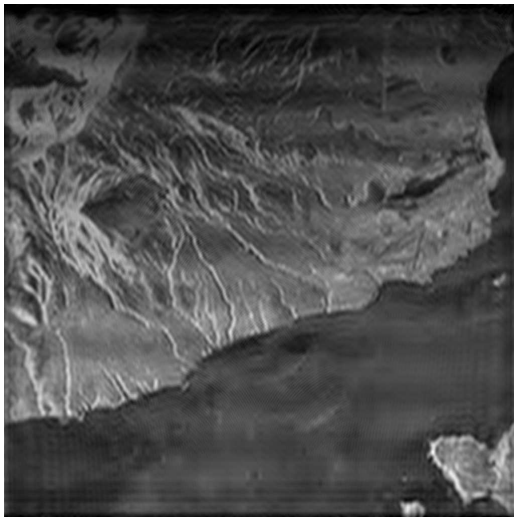


(b)

Fig. 10. Sub-Nyquist range sampling and recovery comparison. (a) Conventional RDA with full Nyquist samples. (b) SAR FISTA (Algorithm 1), $\Psi = I$, using 24% of the coefficients required in conventional RDA.



(a)



(b)

Fig. 11. Sub-Nyquist azimuth sampling and recovery comparison. (a) Conventional RDA with full Nyquist samples. (b) SAR FISTA (Algorithm 2), Ψ is the Daubechies-4 wavelet transform, using 50% of the transmitted pulses.

of the transmitted pulses, which were chosen randomly. This result proves the concept of reduced time on scene.

B. Real Data

To further test the performance of our method and to confirm our model, we conducted simulations on the RADARSAT-1 raw data collected on June 16, 2002, in ascending orbit #34522. The illuminated target is Richmond, Vancouver, Canada. The related key parameters of RADARSAT-1 system can be found in [4]. In this simulation we prove the feasibility of our two-dimensional sub-Nyquist SAR system.

TABLE II
SIMULATED SAR SYSTEM PARAMETERS

| | |
|-------------------------------------|---------------|
| Carrier frequency – f_c | 37.5 MHz |
| Transmitted pulse duration – τ | 1.67 μ s |
| Chirp rate – K_τ | 2.25 GHz/msec |
| Range sampling rate – F_s | 11.25 MHz |
| Sensor velocity – v | 75 km/s |
| Doppler bandwidth | 25 kHz |
| PRF – $1/T$ | 30 kHz |
| Squint angle | 0° |

We simulated two geographically consecutive scenes. The reference image which was taken from an Electro-Optic (EO) satellite is shown in Fig.12(a), the two illuminated scenes are marked in red boxes. In order to simulate the sub-Nyquist system we undersampled the original raw data of each of the scenes. The 3072×4096 matrix was undersampled in both axes. In the range axis we reduced randomly 30% of the coefficients and in the azimuth direction we selected randomly 70% of the columns, which is equivalent to the omission of 30% of the pulses. This leads to a 2150×2867 reduced matrix. Then we use Algorithm 2 in order to reconstruct the images, using the Daubechies-4 wavelet transform as the sparsifying basis. The algorithm parameters are: $\beta = 0.9$, $\lambda = 0.01$, $\bar{\lambda} = 0.001$, $L_f = 1$ and Ψ is taken as the unit transform. The results in Fig. 12 compare the original processing with full Nyquist samples and the sub-Nyquist recovery method using only $0.7^2 = 0.49$ of the original samples in each image. It can be readily seen that despite the missing samples, the detailed images are well reconstructed.

VII. SAR EXPERIMENT

We conclude by presenting a real experiment of our SAR receiver hardware prototype. We integrate our method into a stand-alone system and show that such processing is feasible in practice using real hardware.

A. Our environment

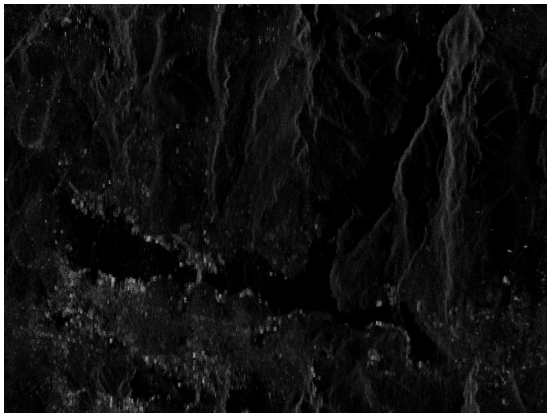
Our setup includes a custom made sub-Nyquist receiver board which implements sub-Nyquist Sampling and digital recovery using Algorithm 1 and Algorithm 2, while the analog input signal (1) was synthesized using National Instruments (NI) hardware.

The experimental process consists of the following steps. We begin by using the AWR software, which enables us to simulate point reflectors with different amplitudes and spatial distribution.

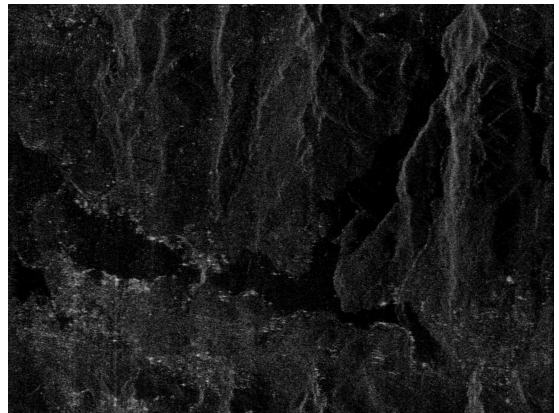
With the AWR software we simulate the complete radar scenario, including the pulse transmission and accurate power loss due to wave propagation in a realistic medium. The AWR also contains a model of a realistic RF receiver, which simulates the demodulation of the RF signal to IF frequencies, and saves the output to a file. However, since AWR is operated only with stationary radar, in order to simulate SAR signals we created the equivalent kinematic state. We simulated the



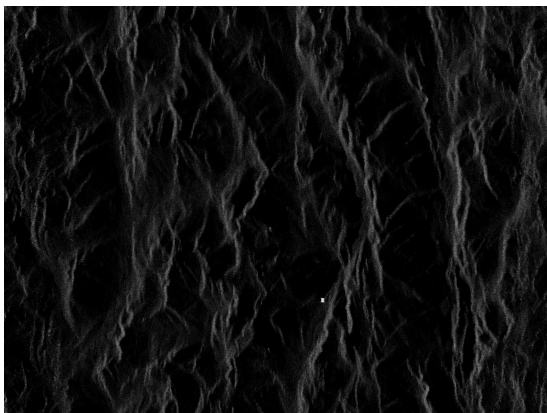
(a)



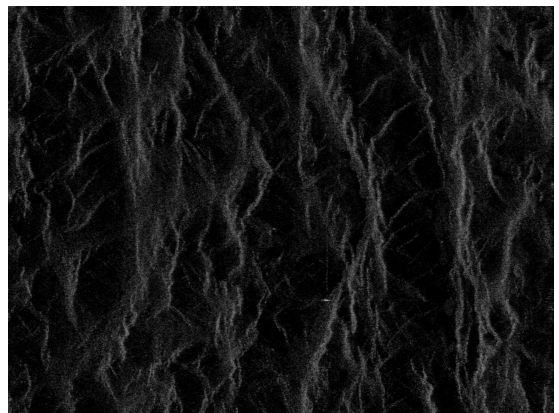
(b)



(c)



(d)



(e)

Fig. 12. Real data simulations using RADARSAT-1 data. (a) A reference electro-optic image with two marked area (in red). (b) The first area (North), processed with full Nyquist samples. (c) The first area processed with Algorithm 2 using only 49% of the original samples, 0.7 rate reduction in each axis. (d) The second area (South), processed with full Nyquist samples. (e) The second area processed with Algorithm 2 using only 49% of the original samples, 0.7 rate reduction in each axis.

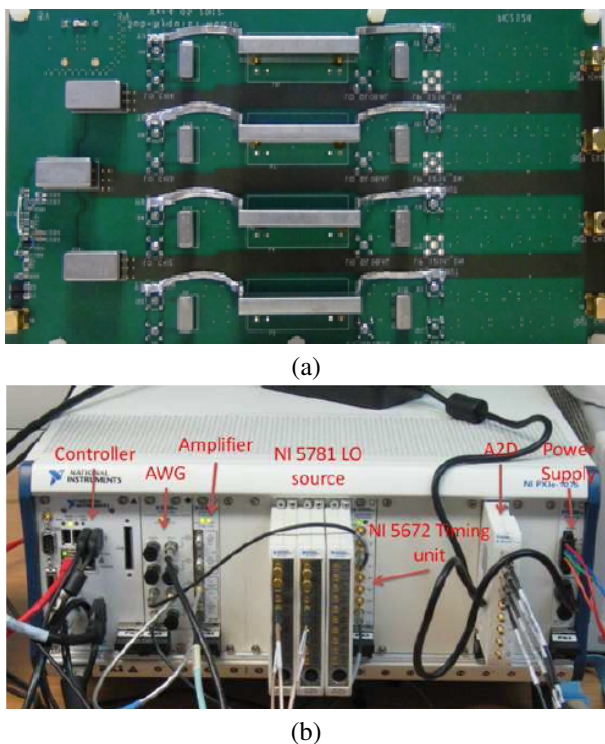


Fig. 13. Sub-Nyquist system. (a) National Instruments (NI) Hardware system. (B) Analog front end 4-channel receiver board.

targets with velocity v , but in the opposite direction than the one that should be to the radar. Our simulation is similar in some manners to ISAR. In ISAR, the radar is stationary and the targets are moving. The angular motion of the target with respect to the radar can be used to form an image of the moving targets. Differential Doppler shifts of adjacent scatters on a target are observed and the targets reflectivity function is obtained through the Doppler frequency spectrum [38].

Next, the generated raw data is loaded to the AWG module, which produces an analog signal. This signal is amplified using the NI 5690 low noise amplifier and then routed to our radar receiver board, which has 4 parallel input channels. Each channel samples a different frequency band, in the following manner: each channel is fed by a local oscillator (LO), which modulates the desired frequency band of the channel to the central frequency of a narrow 80KHz bandwidth band pass filter (BPF). A fifth LO, common to all 4 channels, modulates the BPF output to a low frequency band, and it is sampled with a standard low rate ADC. The LOs are created using three NI 5781 baseband transceivers, acting as trigger based signal generators with a constant and known phase, controlled by NI Flex Rio FPGAs. The AWG also triggers the ADC to sample 250 samples in each sampling cycle, per channel. These samples are fed into the chassis controller and a MATLAB function is launched that runs Algorithm 2. Pictures of the system are shown in Fig.13.

B. Treating noise

In the simulations we adapt the concept of [39] in order to improve the performance in case of noise. We exploit the fact that only the fraction of the spectrum that is actually sampled

should be used for transmission. Thus, we can concentrate the power only in these frequency bands, improving SNR. In addition, our SAR system only needs to transmit a few spectral bands, rather than the whole bandwidth. These bands can be dynamically modified, allowing the radar to adapt to a varying environment and to coexist with communication applications on the spectrum, paving the way to a future cognitive SAR.

We simulated targets which construct an ISAR frame of a moving car, which means that only the car edges can be detected, thus, the image is spatially sparse and Ψ is selected to be the unit transform. We examined 3 scenarios with different SNR: noise free, 5 dB and 2 dB. In each scenario we ran two simulations: a full sampled signal, according to the required by RDA, and a partial sampled signal with only 20% of the required coefficients, using our hardware. The algorithm parameters are: $\beta = 0.85$, $\lambda = 0.001$, $\bar{\lambda} = 0.0001$, $L_f = 25$. For every resulting image, we computed the FSIM index compare to the original full Nyquist sampled reconstructed image without noise. Figure 14 compares the results. Due to the power concentration in the sampled bands which helps to increase the SNR in practice, it can be seen that the FSIM is larger in our method.

This experimental prototype proves that the sub-Nyquist methodology described in this paper is actually feasible in practice. The recovery method proposed here not only describes digital recovery, but also addresses the problem of sampling the analog signal at a low rate, in a way which is feasible with standard RF hardware.

VIII. CONCLUSIONS

We presented a new SAR signal processing algorithm which is equivalent to RDA and showed that the resulting images are similar to those of the conventional processing. The new algorithm exploits the advantages of RDA without the heavy interpolation stage. This allows to perform processing at the Nyquist rate, defined with respect to the effective bandwidth of the signal, which is impossible when the interpolation is performed in time.

Next, we introduced two-dimensional sub-Nyquist sampling and recovery methods, which employ the techniques of Xampling. Moreover, we showed that an image can be reconstructed after dropping a large percentage of the transmitted pulses. We proposed to exploit the complementary pulses in order to capture other scenes during the same CPI. The new CS algorithm leads to fast CS two-dimensional recovery. Using simulated and real data sets, and a Xampling mechanism prototype in hardware, we demonstrated that our technique can cope with practical limitations of computational load and fits real radar imaging problems.

REFERENCES

- [1] M. Soumekh, *Synthetic Aperture Radar Signal Processing*. New York: Wiley, 1999.
- [2] R. Bamler, "A comparison of range-Doppler and wavenumber domain sar focusing algorithms," *Geoscience and Remote Sensing, IEEE Transactions on*, vol. 30, no. 4, pp. 706–713, 1992.
- [3] R. K. Raney, H. Runge, R. Bamler, I. G. Cumming, and F. H. Wong, "Precision sar processing using chirp scaling," *Geoscience and Remote Sensing, IEEE Transactions on*, vol. 32, no. 4, pp. 786–799, 1994.

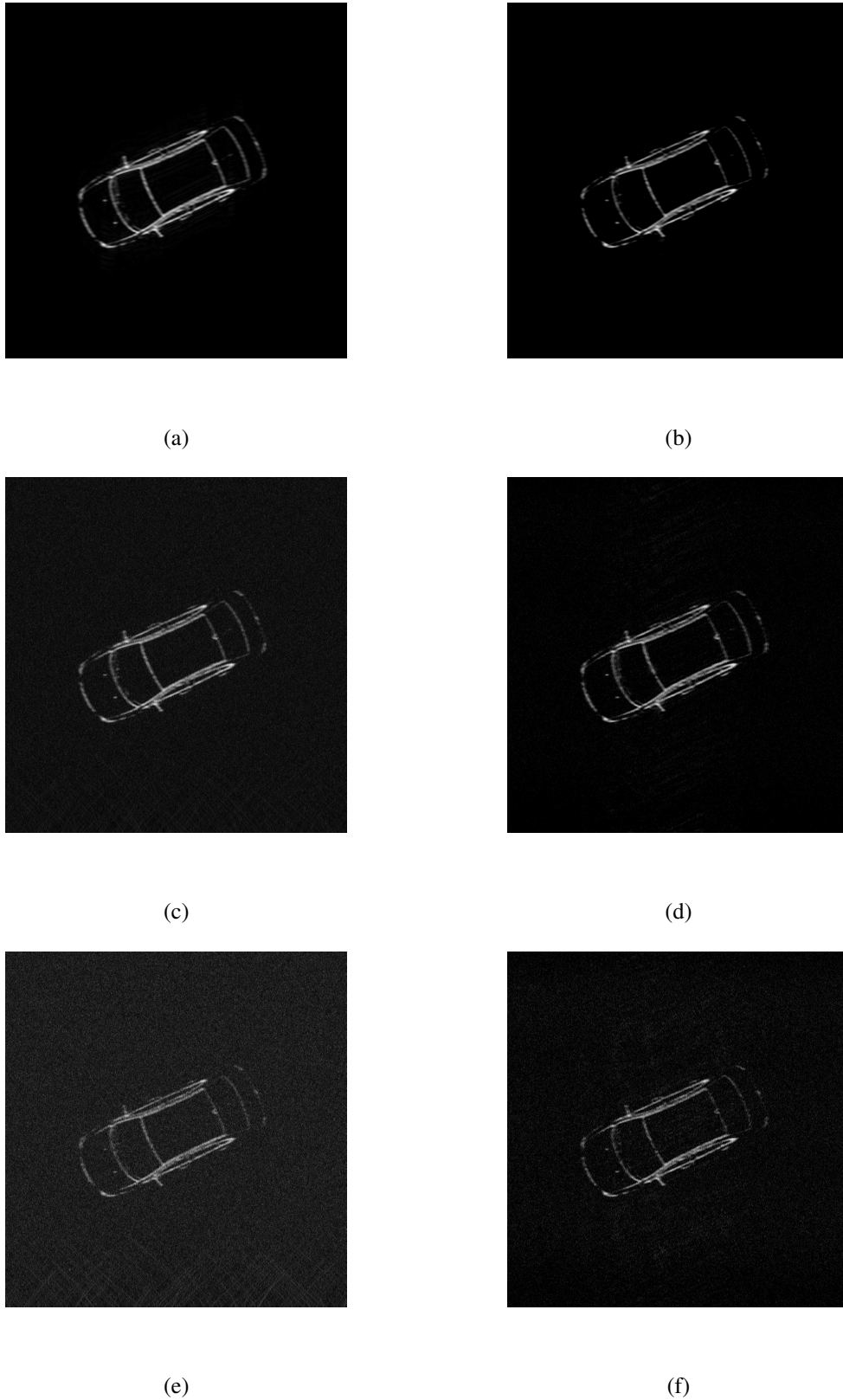


Fig. 14. A SAR experiment using real hardware. Three different noise levels were considered to compare between full-Nyquist processing using conventional RDA and SAR FISTA using only 20% of the samples. (a) Noise free, full-Nyquist samples, conventional RDA processing. (b) Noise free. SAR FISTA. FSIM = 0.9942 (c) SNR = 5 dB. Full-Nyquist samples, conventional RDA processing. FSIM = 0.817 (d) SAR FISTA. using 20% of the original samples. FSIM = 0.842. (e) SNR = 2 dB. Full-Nyquist samples, conventional RDA processing. FSIM = 0.801 (f) SAR FISTA. using 20% of the original samples. FSIM = 0.832.

- [4] I. G. Cumming and F. H. Wong, *Digital Processing of Synthetic Aperture Radar, Algorithms and Implementation*. Artech-House, 2005.
- [5] C. E. Shannon, "Communication in the presence of noise," *Proceedings of the IRE*, vol. 37, no. 1, pp. 10–21, 1949.
- [6] J. C. Curlander and R. N. McDonough, *Synthetic aperture radar*. John Wiley & Sons, 1991.
- [7] Y. C. Eldar and G. Kutyniok, *Compressed sensing: theory and applications*. Cambridge University Press, 2012.
- [8] E. J. Candès and M. B. Wakin, "An introduction to compressive sampling," *Signal Processing Magazine, IEEE*, vol. 25, no. 2, pp. 21–30, 2008.
- [9] Y. C. Eldar, *Sampling Theory: Beyond Bandlimited Systems*. Cambridge University Press, 2015.
- [10] S. Samadi, M. Cetin, and M. Masnadi-shirazi, "Sparse representation-based synthetic aperture radar imaging," *Radar, Sonar & Navigation, IET*, vol. 5, no. 2, pp. 182–193, 2011.
- [11] O. Bar-Ilan and Y. C. Eldar, "Sub-Nyquist radar via Doppler focusing," *Signal Processing, IEEE Transactions on*, vol. 62, no. 7, pp. 1796–1811, 2014.
- [12] E. Baransky, G. Itzhak, N. Wagner, I. Shmuel, E. Shoshan, and Y. C. Eldar, "Sub-Nyquist radar prototype: Hardware and algorithm," *Aerospace and Electronic Systems, IEEE Transactions on*, vol. 50, no. 2, pp. 809–822, 2014.
- [13] Y. C. Eldar, R. Levi, and A. Cohen, "Clutter removal in sub-Nyquist radar," *Signal Processing Letters, IEEE*, vol. 22, no. 2, pp. 177–181, 2015.
- [14] L. C. Potter, E. Ertin, J. T. Parker, and M. Cetin, "Sparsity and compressed sensing in radar imaging," *Proceedings of the IEEE*, vol. 98, no. 6, pp. 1006–1020, 2010.
- [15] M. T. Alonso, P. López-Dekker, and J. J. Mallorquí, "A novel strategy for radar imaging based on compressive sensing," *Geoscience and Remote Sensing, IEEE Transactions on*, vol. 48, no. 12, pp. 4285–4295, 2010.
- [16] J. Fang, Z. Xu, B. Zhang, W. Hong, and Y. Wu, "Fast compressed sensing sar imaging based on approximated observation," *Selected Topics in Applied Earth Observations and Remote Sensing, IEEE Journal of*, vol. 7, no. 1, pp. 352–363, 2014.
- [17] X. Dong and Y. Zhang, "A novel compressive sensing algorithm for sar imaging," *Selected Topics in Applied Earth Observations and Remote Sensing, IEEE Journal of*, vol. 7, no. 2, pp. 708–720, 2014.
- [18] J. Yang, J. Thompson, X. Huang, T. Jin, and Z. Zhou, "Segmented reconstruction for compressed sensing sar imaging," *Geoscience and Remote Sensing, IEEE Transactions on*, vol. 51, no. 7, pp. 4214–4225, 2013.
- [19] N. Wagner, Y. C. Eldar, and Z. Friedman, "Compressed beamforming in ultrasound imaging," *Signal Processing, IEEE Transactions on*, vol. 60, no. 9, pp. 4643–4657, 2012.
- [20] T. Chernyakova and Y. C. Eldar, "Fourier-domain beamforming: the path to compressed ultrasound imaging," *Ultrasonics, Ferroelectrics, and Frequency Control, IEEE Transactions on*, vol. 61, no. 8, pp. 1252–1267, 2014.
- [21] K. Aberman and Y. C. Eldar, "Range Doppler processing via Fourier coefficients: The path to a sub-Nyquist sar", iee radar conference." Philadelphia, PA: IEEE Radar Conference, May 2016.
- [22] M. Mishali, Y. C. Eldar, O. Dounaevsky, and E. Shoshan, "Xampling: Analog to digital at sub-Nyquist rates," *IET circuits, devices & systems*, vol. 5, no. 1, pp. 8–20, 2011.
- [23] T. Michaeli and Y. C. Eldar, "Xampling at the rate of innovation," *Signal Processing, IEEE Transactions on*, vol. 60, no. 3, pp. 1121–1133, 2012.
- [24] M. Mishali and Y. C. Eldar, "Sub-Nyquist Sampling: Bridging Theory and Practice," *IEEE Signal Process. Magazine*, vol. 28, no. 6, pp. 98–124, Nov. 2011.
- [25] D. Cohen and Y. C. Eldar, "Reduced time-on-target in pulse doppler radar: Slow time domain compressed sensing", iee radar conference." Philadelphia, PA: IEEE Radar Conference, May 2016.
- [26] A. Beck and M. Teboulle, "A fast iterative shrinkage-thresholding algorithm for linear inverse problems," *SIAM journal on imaging sciences*, vol. 2, no. 1, pp. 183–202, 2009.
- [27] L. Zhang, L. Zhang, X. Mou, and D. Zhang, "Fsim: a feature similarity index for image quality assessment," *Image Processing, IEEE Transactions on*, vol. 20, no. 8, pp. 2378–2386, 2011.
- [28] S. Boyd and L. Vandenberghe, *Convex optimization*. Cambridge university press, 2004.
- [29] S. Boyd, N. Parikh, E. Chu, B. Peleato, and J. Eckstein, "Distributed optimization and statistical learning via the alternating direction method of multipliers," *Foundations and Trends® in Machine Learning*, vol. 3, no. 1, pp. 1–122, 2011.
- [30] M. V. Afonso, J. M. Bioucas-Dias, and M. A. Figueiredo, "Fast image recovery using variable splitting and constrained optimization," *Image Processing, IEEE Transactions on*, vol. 19, no. 9, pp. 2345–2356, 2010.
- [31] Z. Tan, Y. C. Eldar, A. Beck, and A. Nehorai, "Smoothing and decomposition for analysis sparse recovery," *Signal Processing, IEEE Transactions on*, vol. 62, no. 7, pp. 1762–1774, 2014.
- [32] K. Gedalyahu, R. Tur, and Y. C. Eldar, "Multichannel sampling of pulse streams at the rate of innovation," *Signal Processing, IEEE Transactions on*, vol. 59, no. 4, pp. 1491–1504, 2011.
- [33] I. C. Cumming and J. R. Bennett, "Digital processing of seasat sar data," in *Acoustics, Speech, and Signal Processing, IEEE International Conference on ICASSP'79*, vol. 4. IEEE, 1979, pp. 710–718.
- [34] P. Stoica and P. Babu, "Sparse estimation of spectral lines: Grid selection problems and their solutions," *IEEE Transactions on Signal Processing*, vol. 60, no. 2, pp. 962–967, 2012.
- [35] S.-J. Wei, X.-L. Zhang, J. Shi, and G. Xiang, "Sparse reconstruction for sar imaging based on compressed sensing," *Progress In Electromagnetics Research*, vol. 109, pp. 63–81, 2010.
- [36] T. Wimalajeewa, Y. C. Eldar, and P. K. Varshney, "Recovery of sparse matrices via matrix sketching," *arXiv preprint arXiv:1311.2448*, 2013.
- [37] M. Younis, C. Fischer, and W. Wiesbeck, "Digital beamforming in sar systems," *Geoscience and Remote Sensing, IEEE Transactions on*, vol. 41, no. 7, pp. 1735–1739, 2003.
- [38] D. R. Wehner, "High resolution radar," *Norwood, MA, Artech House, Inc., 1987, 484 p.*, vol. 1, 1987.
- [39] D. Cohen and Y. C. Eldar, "Towards sub-Nyquist cognitive radar", iee radar conference." Philadelphia, PA: IEEE Radar Conference, May 2016.